

THE JetCurry CODE. I. RECONSTRUCTING THREE-DIMENSIONAL JET GEOMETRY FROM TWO-DIMENSIONAL IMAGES

KUNYANG LI¹, KATIE KOSAK^{1,2}, SAYALI S. AVACHAT¹, ERIC S. PERLMAN

Department of Physics and Space Sciences, 150 W. University Blvd., Florida Institute of Technology, Melbourne, FL 32901, USA

Draft version February 3, 2017

ABSTRACT

We present a reconstruction of jet geometry models using numerical methods based on a Markov Chain Monte Carlo (MCMC) and limited memory Broyden - Fletcher - Goldfarb - Shanno (BFGS) optimized algorithm. Our aim is to model the three-dimensional geometry of an AGN jet using observations, which are inherently two-dimensional. Many AGN jets display complex hotspots and bends over the kiloparsec scales. The structure of these bends in the jets frame may be quite different than what we see in the sky frame, transformed by our particular viewing geometry. The knowledge of the intrinsic structure will be helpful in understanding the appearance of the magnetic field and hence emission and particle acceleration processes over the length of the jet. We present the method used, as well as a case study based on a region of the M87 jet.

Keywords: galaxies: jets, galaxies: structure, galaxies: individual(M87), methods: numerical

1. INTRODUCTION

In active galactic nuclei (AGN), relativistic jets transport energy and mass from the sub-parsec central regions to Mpc-scale lobes, with a kinetic power comparable to that of the host galaxy and the AGN, profoundly influencing the evolution of the host, nearby galaxies and the surrounding interstellar and intracluster medium (Silk et al. 2012; Fabian 2012). The generation of these flows is tied to the process of accretion onto rotating black holes, where the magneto-rotational instability can couple the black hole's spin and magnetic field to produce high-latitude outflows close to the speed of light (Meier et al. 2001). While these jets have a dominant direction of motion (i.e., outward from the black hole) they often have bends, as well as features within them that are either perpendicular to or aligned relative to the jet at some angle. Deciphering the true nature of these features, their geometry and their relation to and dynamical meaning within the flow is a difficult problem, as any astronomical image we take is of necessity a two dimensional (2-D) view of a three-dimensional (3-D) object.

The problem of reconstructing three-dimensional information from 2-dimensional images is one that is common to many fields, but it is particularly critical in astronomy. In most other cases, for example medical imaging, one may take images of a source from multiple points of view to aid in the reconstruction. However, that is not possible in astronomy, so we must rely on other methods. For example, Steffen et al. (2011), Wenger et al. (2012), Wenger et al. (2013) and Cormier (2013) used symmetries inherent in, respectively, planetary nebulae and galaxies, plus two-dimensional images, to infer and reconstruct three-dimensional visualizations of those objects. This field is, in fact, rapidly growing in astronomy, as can be seen by the vast number of subjects explored on the 3DAstrophysics blog³.

In jets, the problem is rather different. Unlike in galaxies or planetary nebulae, we cannot make assumptions such as spherical, elliptical or disk symmetry, or rotation. However, we can assume a dominant direction of propagation. As an example of the typical knotted structure of AGN jets, we show in Figure 1 a broad view of the M87 jet, one of the nearest of the class at 17 Mpc distance, taken from Meyer et al. (2013). As can be seen, in even a single image the M87 jet shows an amazing complexity of features, including knots, helical undulations, shocks, and a variety of other things, many of which are oriented at some odd angle with respect to the overall jet direction. Some of these features are seen to move, as shown for the M87 jet by Meyer et al. (2013), who showed that features with apparent velocities up to about $6c$ are seen within the inner $12''$ of the jet, with a general decline in apparent speed with increasing distance from the nucleus, although there are also some nearly stationary components, largely located near the upstream ends of knots. In addition, the polarimetric imaging of (Avachat et al. 2016) shows apparent helical winding structures to the inferred magnetic field vectors in several knots. These features are clues to complex jet dynamics, but are difficult to interpret properly.

In this paper, we describe a geometrically based code that attempts to use astronomical images of jets to reconstruct their three-dimensional structure. This is an evolving project that in later stages will attempt to use kinematic information as well as incorporate special relativistic corrections so that foreshortening, Doppler boosting, and other effects can be included. Our goal is to provide a firmer geometrical grounding to these modeling efforts by allowing reconstruction of a jet's structure (both total flux and polarization) in three dimensions.

2. MODEL

We use parametrized equations in 3 dimensions to describe the geometry of the jet. The key parameters we need to consider are the distance between any two features and the apparent angle between them with respect to the direction of the jets axis. We assumed that the

¹ These authors contributed equally

² Current Address: Physics Department, University of Warwick, Coventry, CV4 7AL, UK

³ <https://3dastrophysics.wordpress.com/>

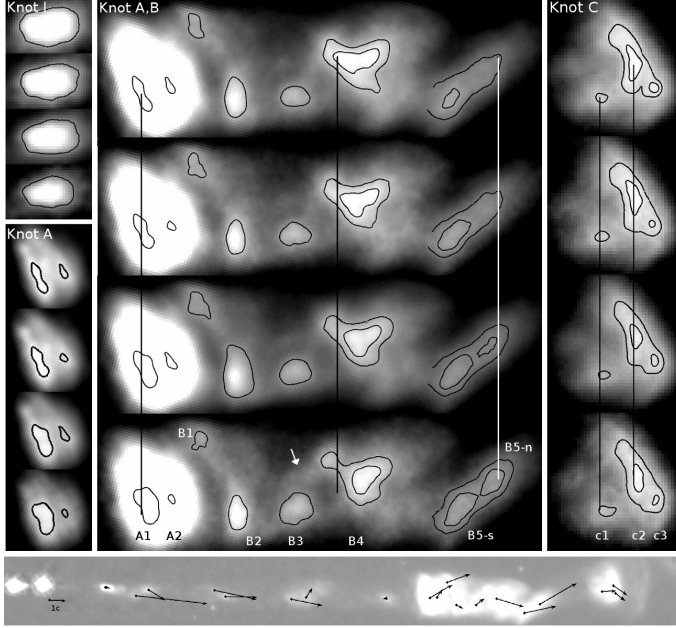


Figure 1. Superluminal motion of the sub-components in several of the knot regions of the M87 jet, spanning over 13.25 years of monitoring between 1995–2008, with the *Hubble Space Telescope*. The westward direction lies 20.5° below the horizontal. The bottom panel depicts the velocities as vectors from their positions in the jet. The length of the vectors is proportional to the apparent speed. Reproduction of Figure 3 of Meyer et al. (2013). Courtesy-Eileen Meyer.

2-D projection of the jets axis lies along the x -axis and measured the angles with respect to the positive x direction. We considered these two as known parameters, which we can directly measure from the images, i.e. in the sky frame. A third parameter, assumed to be known (albeit from other information such as a $\beta - \theta$ plot based on observed superluminal motion), is the angle the jet's propagation axis makes with respect to the LOS. To simplify the model both computationally and physically, we assume that the jet is non-relativistic. The LOS effects in addition to the relativistic Doppler boosting can enhance the intensity and shift the frequency observed, as well as change the comparison between geometry in the jet and observer frames. However, we are also working on the next generation of this model, which will include the relativistic treatment.

2.1. Description of the Geometry

Following Conway & Murphy (1993), Figure 2 shows the relevant geometry for a single bend within a jet, and specifically how the 2-D sky frame can be related to the jet's frame, which is inherently 3-D. All primed points represent the observed, sky-frame projection we see, with the components lying at A' and B' in that frame but at points A and B in the jet's frame. The point D' is the projection of B' on the $+x$ axis, and the point D is projection of B on xz plane. η is the angle formed by segment $A'B'$ with the $+x$ axis. The point C is such that the $\angle CAB$ is ξ . Segment CB makes an angle ϕ with the xz plane (i.e. $\angle BCD = \phi$). This way, $\triangle ABC$ is raised off the xz plane through angle ϕ , while the segment AC still lies in the xz plane. Segment AC makes an angle θ with the line of sight (LOS), which is assumed to be along $+z$ axis. The distance

between points A and B in the jet's frame is d , while s is the projection of d on the xy plane, i.e. the distance between A' and B' . α is the apex angle of $\triangle BAD$, and β is the angle between triangles BAD and FAE . Finally, $\triangle AGH$ is the projection of $\triangle ABD$ on the yz plane.

2.2. Non-linear Parametrized Equations

We use a set of non-linear parametrized equations containing the angles and distances described above. Assuming the non-relativistic jet flow and using the geometry in Figure 2, we derive the following non-linear equations including three known parameters (η, s, θ), and five unknown ones ($\alpha, \beta, \xi, \phi, d$).

1. If the local jet structure has a smaller bend i.e. $\xi < \frac{\pi}{2} - \theta$, the transformation is:

$$\tan \eta = \frac{\sin \xi \sin \phi}{\cos \xi \sin \theta + \sin \xi \cos \phi \cos \theta} \quad (1)$$

$$\frac{s}{d} = \cos \beta \quad (2)$$

$$\left(\frac{\tan \beta}{\tan \alpha} \right)^2 = \cos^2 \eta \quad (3)$$

$$d \cos \xi \cos \theta = s \cos \eta \tan \alpha + d \sin \xi \cos \phi \sin \theta \quad (4)$$

$$d^2 = s^2 \left[\frac{\sin \eta}{\sin \phi} \right]^2 + s^2 \left[\frac{\cos \eta}{\cos \alpha} \right]^2 \sin^2(\theta + \alpha) \quad (5)$$

2. If the local jet structure has a larger bend i.e. $\xi \geq (\frac{\pi}{2} - \theta)$, the equations (4) and (5) modify as:

$$d \cos \xi \cos \beta + s \cos \eta \tan \alpha = d \sin \xi \cos \phi \sin \theta \quad (6)$$

$$d^2 = s^2 \left[\frac{\sin \eta}{\sin \phi} \right]^2 + s^2 \left[\frac{\cos \eta}{\cos \alpha} \right]^2 \sin^2(\theta - \alpha) \quad (7)$$

Our aim is to solve for the angles ξ, ϕ, α, β , and the distance between the knots d . The system is under-determined, and so cannot be solved exactly. However, as we shall describe, by making use of the angle η , distance s and angle of LOS θ as known parameters, we can derive the solution space as well as the relative probability of various bend parameters.

Please note that Conway & Murphy (1993) did not give either these equations or a derivation of them, nor did they try to derive more detailed 3-D information about any individual jets. Their aim was instead to attempt to understand in a geometrical sense the misalignment of arcsecond-scale features in blazar jets with the features seen on milliarcsecond scales by VLBI arrays. As with this work, they also did not attempt to include relativistic effects, an issue we are now working to remedy with a future refinement of this code.

3. JETCURRY

We present a Python code to model 3-D jet geometry of an AGN jet from its 2-D image. Our code is available for free in an IPython notebook platform on Github ⁴. The code incorporates the use of a nonlinear solving algorithm (*emcee*), as well as Python packages: NumPy,

⁴ <https://github.com/esper1man/JetCurry>

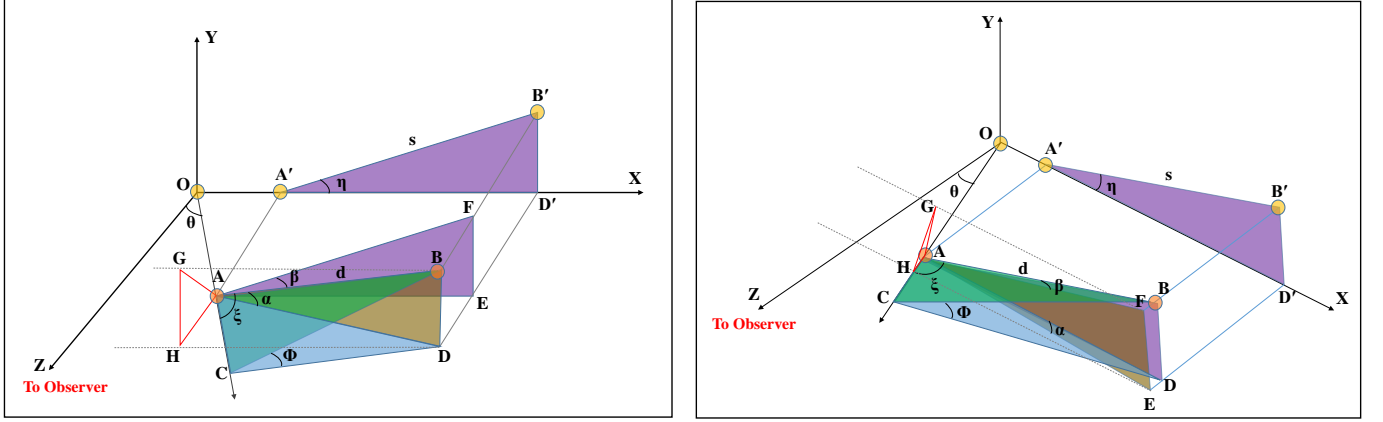


Figure 2. Geometry of the jet in 2 and 3 dimensions. Left: For $\xi < \frac{\pi}{2} - \theta$; Right: For $\xi \geq \frac{\pi}{2} - \theta$. The jet lies at an angle θ from the line of sight which is assumed along z axis. The projection of the jet in sky frame lies in the xy plane. The points A, B and A', B' represent any two knots in the jet's frame and sky frame respectively. Point O is an origin and represent the starting point of each iteration of the code. Please see the text for the description of various angles shown.

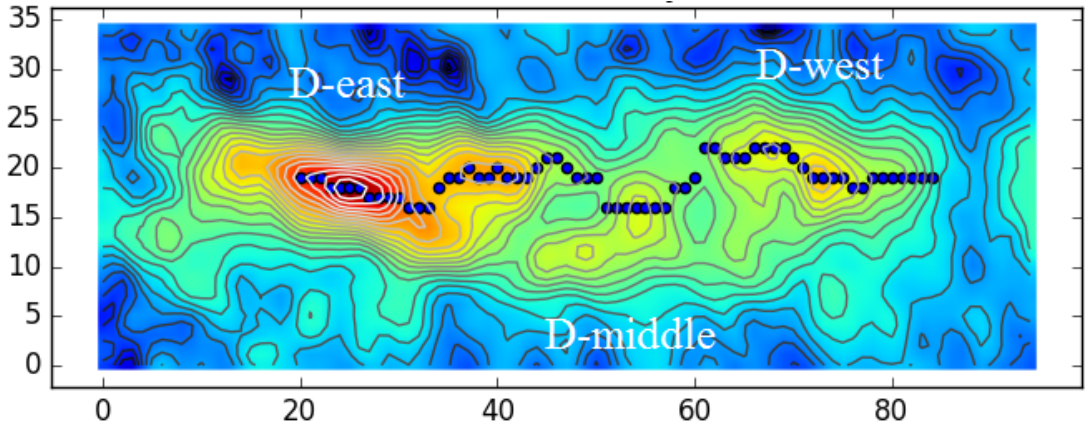


Figure 3. Outline of knot D in M87's jet. As in Figure 1, the westward direction lies 20.5° below the horizontal. A square root filter is applied to the color scale. The axes are labeled in pixels (1 pix = $0.''025$ arcsec = 1.95 parsec) The points in the blue show a highest flux fit in each column using a spline fit. For details see § 5.1.

AstroPy (Astropy Collaboration et al. 2013), Matplotlib (Hunter 2007), SciPy (Jones et al. 2001) and the optional VPython (Shreher et al. 2000).

The code has a user-defined initial part of the jet which will act as the reference or origin point for the further calculations. Starting at the reference point, the code finds the position of the highest flux within 4 columns (a bin) of data in the image matrix and fits along the x axis for the general location of the bends in the jet. To smooth out the resulted jet stream, a spline fitting is used. We ran JetCurry on an optical image of knot D in M87's jet, chosen as an example of small region of a relatively complex jet. This was done because the knots have varying and complex flux structure and are separated by considerable distances and hence the jet stream is better modeled by focusing on individual knot regions at a time instead of the entire jet, as the model can wander in regions in between knot complexes.

In Figure 3, the image of knot D is shown with the fit of the maximum flux values along the jet starting at the user-defined reference point. By this method, the highest flux portion of the jet stream is properly outlined for further use in calculations. Importantly, while a bent structure can be seen, we do not know the nature

or orientation of each of the apparent bends, and as a result we cannot directly derive component lengths, bend parameters, or quantities that depend directly on these things, such as volume emissivities and the like.

3.1. Non-linear Solvers

From the observed image in 2-D, we can only measure angles η and distances s , as shown in Figure 2. We assume that the LOS viewing angle (θ) for M87's jet is 15° with respect to the observer (Biretta et al. 1999; Perlman et al. 2011). The model then uses equations 1-7 to solve for the most probable values of the unknown parameters, α , β , ϕ , ξ , and d using a non-linear solver, *emcee*, to explore the solution space. *Emcee* (Foreman-Mackey et al. 2013) is a highly efficient, open-source Python package that uses a Goodman & Weare affine-invariant MCMC Ensemble Sampler, aiming to find a global minimum solution. We are using MCMC methods because of the underdetermined nature of the solution space, particularly because of the complex nature of our non-linear trigonometric equations. To save on computational time, we use a generic initial guess to find solutions in the first trial of *emcee*. After this, the previous results are set as the initial guess of the next trial until a more defined range of

possible solutions is found. The number of times *emcee* is run depends on the user-preference (we have chosen to do it twice).

Once *emcee* has located the global minima/maxima regions, we use a nonlinear solver. To ensure the solutions of the variables are real, we take the logarithm of the equations. We found the limited memory BFGS algorithm (Broyden 1970; Fletcher 1970; Goldfarb 1970; Shanno 1970) converges to the real solution faster and more accurately in our test cases compared to other nonlinear solvers. The algorithm is in the same class as Quasi-Newton methods and hill climbing with bounds on the solutions and can be applied to a general non convex function that has continuous second derivatives. The bounds in the nonlinear solver are by default in JetCurry set to be within 10 steps of nonlinear solver. We present further details of our case study of knot D in § 5.

4. TESTING JETCURRY

To test the accuracy of JetCurry, we created a mock bend using the model parameters (ϕ, ξ, θ, d) . The values of ϕ and ξ were restricted to the range $[0, \pi]$ and $[0, \pi/2]$, respectively. We assume that bends greater than 90° are most probably unrealistic. The set of values used for testing were $\phi = [15^\circ, 30^\circ, 60^\circ, 90^\circ, 120^\circ, 150^\circ]$, and $\xi = [10^\circ, 15^\circ, 30^\circ, 45^\circ, 60^\circ, 75^\circ]$; creating 36 pairs of (ϕ, ξ) . We then set $d = 100$ pc and LOS angle $\theta = 15^\circ$ and calculate a range of values of (η, s) , which are the measurable variables in our model. The resulting (η, s) are then plugged back into our model to test how well we can reproduce the given (ϕ, ξ) .

The resulting values of ϕ , ξ , and d are represented as an error distribution plot shown in Figure 4. The absolute error distribution is shown by the color bar on the right in each panel. As shown, JetCurry fails to give accurate results at larger ϕ and smaller ξ values (seen in red). In the ranges of $\phi > 90^\circ$ and $\xi < 20^\circ$, the error can be as large as 250%. This is due to the nature of the equations, and particularly where the expressions in the denominator have singularities. This makes the probability distribution in these regions complex and as a result, MCMC methods cannot efficiently work backwards to find the global minima.

Figure 5 shows the corner plot of the marginalized total probability distribution of α , β , ϕ , ξ , and d from the JetCurry result when use $\eta = 38.4^\circ$, $s = 14.0$ pc, and $\theta = 15^\circ$ as input, where η and s are calculated from the mock bend structure with parameters set as $(\theta, \phi, \xi, d) = (15^\circ, 150^\circ, 10^\circ, 100$ pc). The solution vector at the location of maximum a posteriori probability (MAP) is $(\alpha, \beta, \phi, \xi, d) = (41.2^\circ, 37.8^\circ, 83.6^\circ, 38.9^\circ, 19.3$ pc). The absolute errors in ϕ , ξ , d are 66.4° , 28.9° , 80.7 pc. This corner plot illustrates the complex structure of the total probability distribution in 5-dimensional parameter space, which together with the large step size used to explore the parameter space, explains the large absolute error due to optimization inefficiency when trying to recover the 3-D mock bend structure set with large ϕ and small ξ using JetCurry. For error in d , the complex structure of the probability distribution is the main reason. As shown in the bottom row of the corner plot, a deep local minimum at $d \approx 20$ pc prevents the walkers from finding the more likely result at $d = 100$ pc.

Another important feature in the corner plot worth

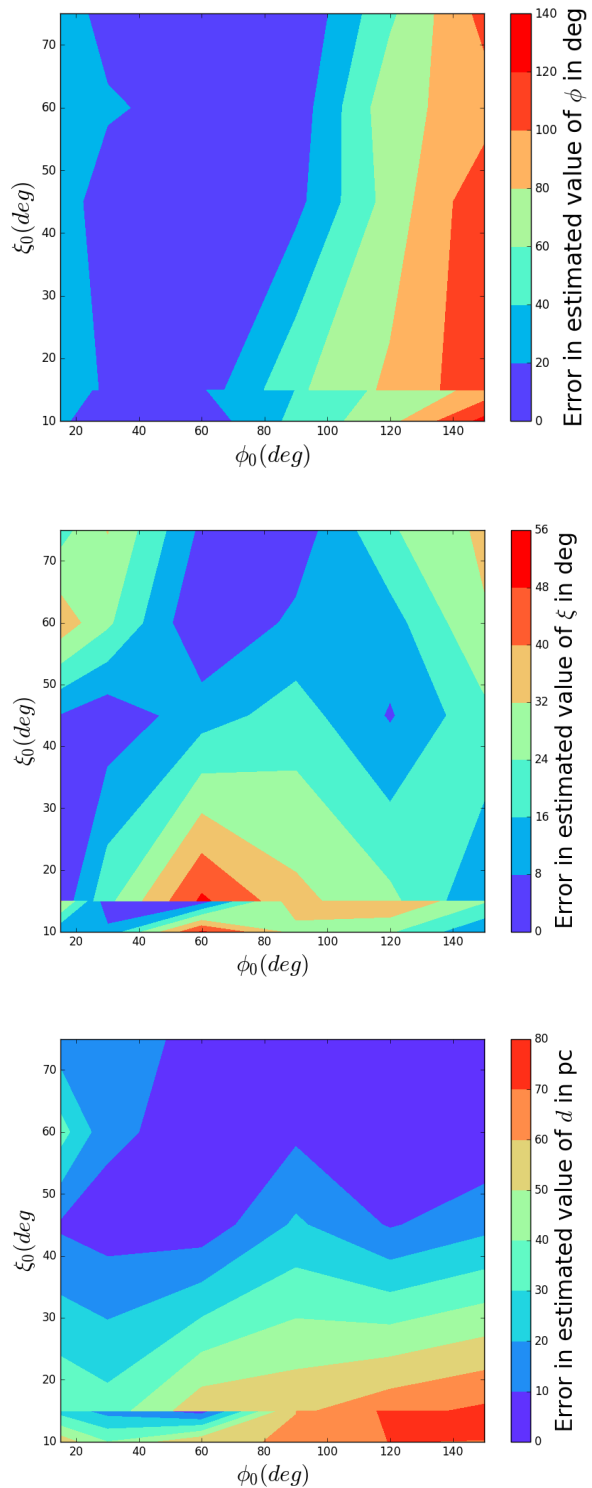


Figure 4. Absolute error distribution of estimated values of ϕ (top), ξ (middle) and d (bottom) on (ϕ_0, ξ_0) parameter space.

mentioning is the bipolar shape of the probability distribution of ϕ . There are two potential bend structures that give the same projection in sky frame when $\xi < \frac{\pi}{2} - \theta$ (i.e. $\xi < 75^\circ$ in the case of the M87). One potential structure is when $\phi \in [0, \pi/2]$, the other is when $\phi \in [\pi/2, \pi]$. However, these two bend structures are

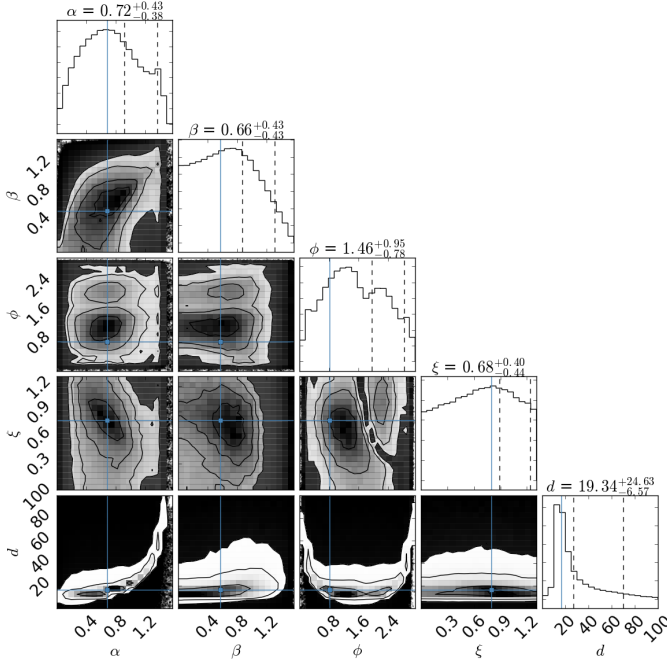


Figure 5. Corner plot showing the marginalized total probability distribution of α , β , ϕ , ξ , and d from the JetCurry result when use $\eta = 38.4^\circ$, $s = 14.0$ pc, and $\theta = 15^\circ$ as input, where η and s are calculated from the mock bend structure with parameters set as $(\theta, \phi, \xi, d) = (15^\circ, 150^\circ, 10^\circ, 100$ pc). The solution vector at MAP is $(\alpha, \beta, \phi, \xi, d) = (41.2^\circ, 37.8^\circ, 83.6^\circ, 38.9^\circ, 19.3$ pc). The absolute errors in ϕ , ξ , d are 66.4° , 28.9° , 80.7 pc. The grey scale in this plot represents the number of iterations at points in the parameter space.

not equally likely to due to both model equations 1 - 7 and the range that constrains ξ , which possibly explains uneven bipolar probability distribution of ϕ . This also explains the bipolar probability distributions of the α , β , ξ and d subplots against ϕ in the Figure 5. The trigonometric functions, especially like ‘tangent’, make the model equations highly non-linear and cause such complex structure of probability distributions.

The testing shows us that JetCurry can be accurately applied to the bends in the jet where $0 < \phi < 90^\circ$ and $20^\circ < \xi < 90^\circ$, to reproduce the 3-D structure successfully. However, it cannot recover the bend structure accurately for values of ϕ and ξ out of these ranges.

5. RESULTS

We now present a case study of a small region of the M87 jet (knot D, shown in Figure 3), which displays a complex morphology. The optical image used for this search was taken from (Avachat et al. 2016), and has a scale of $0.025''/\text{pixel}$, translating to 1.95 pc/pixel at M87’s distance of 16 Mpc. The knot has 3 sub-components, namely, D-east, D-middle and D-west, as well as multiple apparent bends. Knot D-east appears to be at an angle from the northern edge of the jet cross-section to the southern edge over a distance of about 25 pixels ($\sim 0.625''$). Near its downstream end, it appears to split into northern and southern branches, out of which the southern branch is brighter and has been identified as knot D-middle. Here the spline fit shows two fairly sharp bends. These two bends connect knot D-middle to the northern branch of D-east’s downstream end and

D-west’s upstream end, which lies closer to the northern edge of the jet.

5.1. Spline curve fit and Corner plots

Using the 45 flux maxima locations obtained from Gaussian fitting in each bin of pixel columns, we fit a spline curve to the entire region (Figure 3). The main code takes in the values of η and s measured along the streamline shown, as known along with the LOS angle θ (which we assume is 15°) and outputs the range of values for each unknown parameters i.e. angles α , β , ϕ , ξ and the distance d , by solving the non-linear equations 1 through 7. To plot the posterior probability distribution of the values of unknown parameters, we make corner plots for each flux maximum or bend in the knot (similar to Figure 5). Each corner plot is a multi-dimensional representation of projections of the posterior probability distribution of parameter space (Foreman-Mackey 2016). We interpret the maximum of the probability distribution (MAP) as the actual solutions of angle and distances, although this can be subject to irregularities near places where a function is discontinuous or nonlinear (see e.g., §5.3). The grey scale represents the output probability in parameter space, with higher probabilities corresponding to darker colors.

5.2. Solutions in Three Dimensions

We further convert the angles obtained from our main modeling code to the three dimensional Cartesian coordinates (x, y, z) , in order to be able to plot them in three dimensions. The (x, y, z) coordinates found this way make use of the most probable values taken from the corner plots obtained for each bend. We use the following conversion equations, in terms of angle parameters α , β , ϕ , ξ and distance d between the two respective bends, to obtain the required (x, y, z) coordinates -

$$\begin{aligned} x &= d \cos\eta \cos\beta + 15 \\ y &= d \sin\eta \cos\beta + 13 \\ z &= d \cos\eta \cos\beta \tan\alpha \end{aligned} \quad (8)$$

We add 15 and 13 to the equations of x and y respectively, because we assumed the origin to be at $(15, 13)$, i.e. the upstream end of the knot D, instead of the actual origin $(0, 0)$ of the image in Figure 3.

5.3. VPython Visualizations

To further validate our results, we make a projection of the Cartesian coordinates of the bend vertices, of the sky as viewed from Earth to the two dimensions i.e. on to the xy plane. To get the projection, we used the same equations for x and y as in eq. 8, and assumed $z = 0$. We then overlay the scatter points in two dimensions on the spline curve fit image of Figure 3. The overlay is shown in Figure 6. By comparing the scatter point curve and spline fit curve, we see that the two coincide well, particularly in the latter part of knot D ($x > \sim 30$ pixels), but is poorer at the upstream end (first 8-10 points), however. We believe that this indicates instability in the code in its first few runs due to the fact that the non-linear equations include the tangent function and these few points make an angle η which is close to 90° , where $\tan\eta$ (see §4) is mathematically not defined. However, as

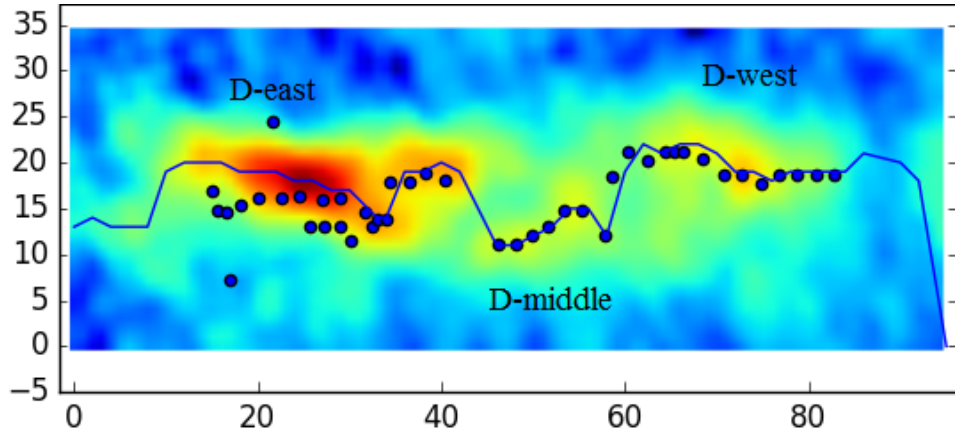


Figure 6. Overlaying the 2 dimensional projection of cartesian coordinates and spline curve fit on the total flux image of knot D shown before as Figure 3. The blue line, overlaid on to the blue points, represents the coordinate fit.

the code iterates along the jet, the solutions became more and more stable, particularly as η gets further away from 90° . The fit is therefore less reliable in this range.

For visualization, we made a three dimensional model in VPython using the (x, y, z) coordinates of eq. 8. VPython is an open-source module run on a Jupyter IPython Notebook to create 3-D images. Each point (shown in red) on Figure 7 is a combination of the most probable values of ϕ , ξ and d for each bend. The envelope of these points should not be viewed as a trajectory, however, as that is likely more gently curved. Here we show rotations of this projection, obtained using VPython visualization.

Figure 7 show rotations of projection, obtained using the VPython visualizations of knot D. It is useful to investigate the possible nature of the apparent bends in the knot using this visualization. The blue points on the image of knot D (in xy plane) are the spline fit flux maxima locations in Figure 6 while the red points in the 3-D space represent the most probable solutions of non-linear parametrized equations described in §2.2. The red dotted lines connect the red points to the blue points shows the projections as a guide to the eye. The radii of the blue and red points represent the errors in the flux fit and most probable solutions of equations, respectively. The red dotted lines do not precisely coincide with the blue points on the image due to the uncertainty in the solutions of the non-linear equations and a possible degeneracy in the bipolar nature of the probability distribution (as explained in §4).

The 3-D deprojection shown in Figure 7 of the bends in knot D complex are much more complex than what we see on the sky plane in 2-D (refer to figure caption for the locations of sub-components of knot D). The smaller bend in D-east looks smooth and shows a slow gradient southward in the sky frame, however, viewed in 3-D shows many small rapid turns, inward and outward of the page as can be seen in the Figure. The larger bend between D-east and D-middle displays a sharp apparent turn downward. However, in three dimensions, our model predicts that it is located inward as well as downward. The bend between D-middle and D-east is a similar sharp turn upward on the sky plane, however, in three dimensions the flux maximum is located near the front surface of the jet. We can also see 3 smaller bends within

D-middle, which lie close to the line of sight and hence cannot be seen in the two dimensional projection. At the end of knot D complex, in D-west, we see a few small bends, but most of the knot does not show much variations in the flux maxima structure in two dimensions. However, our model indicate that these small bends may be quite sharp in three dimensions. Since this region lies in the parameter space where our testing (§4) indicates lower accuracy due to the non-linearity of the equations (also evident in the larger non-correlation between blue and red points), we emphasize that caution is warranted here.

The orientations of bends as seen inward and outward with respect to the cross-section of jet perpendicular to our line of sight may be indications of a possible helical nature of the filamentary structure discussed in previous works (such as Owen et al. (1989); Hardee & Eilek (2011); Perlman et al. (2011)). To examine this further, we show in Figure 8 an overlay of the fit points and spline fit on to the polarization (MFPA) vectors in the region of knot D (polarization image taken from Avachat et al. (2016)). The maxima of polarization is observed to lie about $0.2 - 0.5$ arcsec downstream of the flux maxima; however, the projected scatter plot points are seen to follow the orientations of the polarization vectors in the knot. It is interesting that, except for the first 8-10 points (discussed previously), the apparent rotations of the polarization vectors are followed very well by the model fits. For example, in knot D-east δ , at $(3.25, 0)$ arcsec in Figure 8, the polarization vectors are observed to turn clockwise downward. The spline fit curve as well as the projected scatter points are seen to have a similar orientation at this location. We see a similar feature further downstream in D-west β , at $(4.1, 0)$ arcsec and D-West γ , at $(4.2, 0)$ arcsec in Figure 8. The MFPA vectors in β are seen to curve back upward whereas in γ , the vectors turn clockwise again and are oriented oblique near the edge of the jet. The spline fit curve as well as projected coordinates have similar orientations as polarization vectors in most of these regions, demonstrating that the solutions obtained using our model are reasonable.

6. CONCLUSIONS

The radio and optical polarimetry images presented in Avachat et al. (2016) clearly show apparent helical

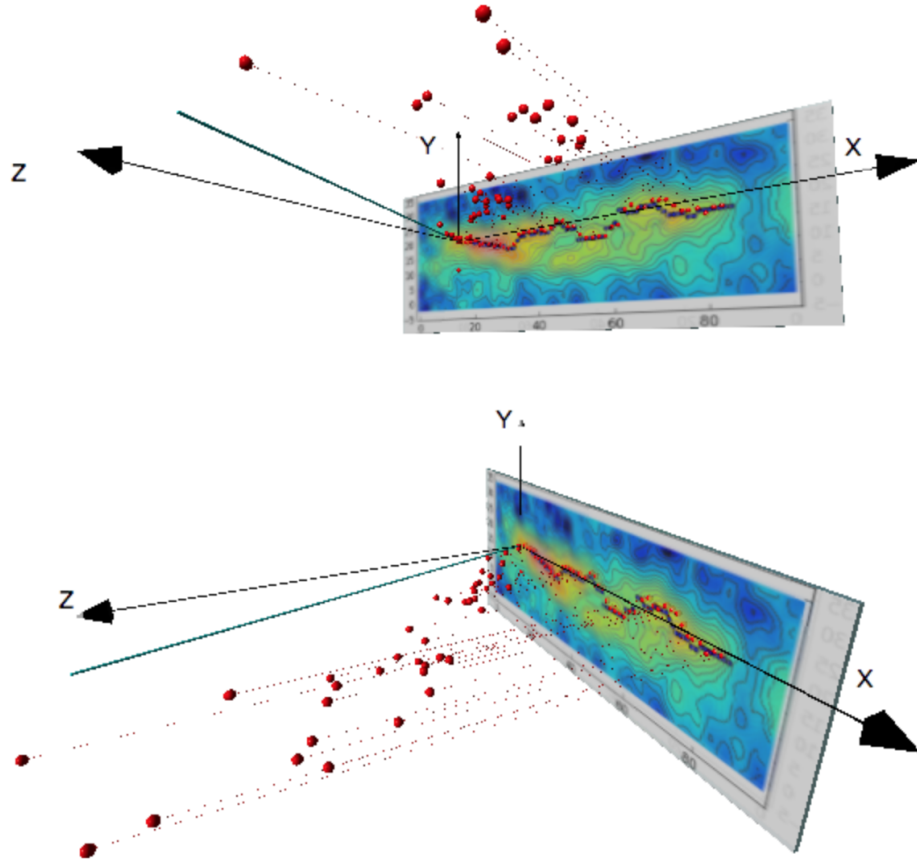


Figure 7. VPython visualizations of knot D complex from two different perspectives. The blue point overlaid on the image represent spline fit of flux maxima while red points in the 3-D space represent the most probable solutions of the non-linear parametrized equations. The red dotted lines connecting the blue and red points act as a guide to the eye to follow the projections from 2-D to 3-D. The scale on the image corresponds to 4 pixels = 0.1 arcsec. The line of sight lies along the cyan line drawn at 15° from the z axis and lies in the xz plane. Knot D-east lies between ≈ 15 -40 pixels, D-middle lies between ≈ 40 -60 pixels and D-west lies between ≈ 60 -80 pixels on this image.

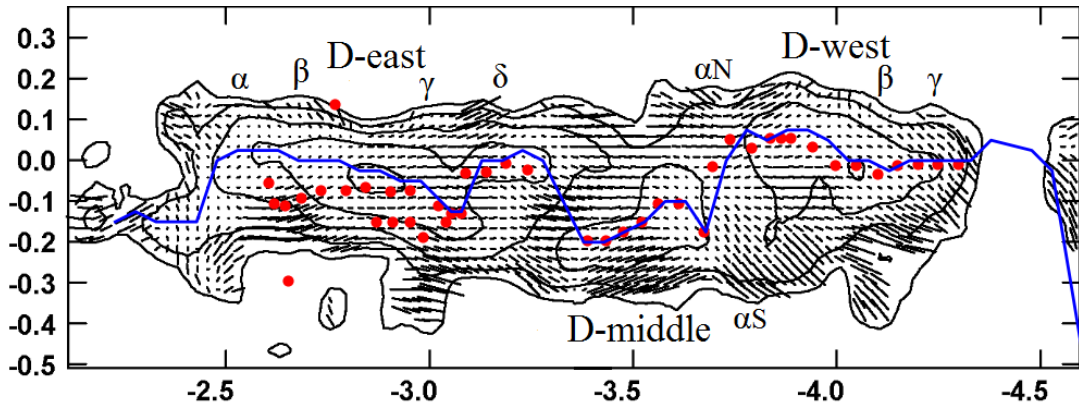


Figure 8. Overlaying the 2 dimensional projection of cartesian coordinates and spline curve fit on the polarization (MFPA) vector image of knot D. The blue line, overlaid on to the high flux points in red, represents the coordinate fit, similar to the one shown in Figure 6.

structure throughout the jet. Especially in knots HST-1, D, A and B (their figures 3, 4, and 6), we see a double helical pattern which most possibly are a signature of underlying helical structure and possibly the magnetic field along the jet. In general, all the knots in the jet show filamentary features throughout along with apparent wrappings around the edges of the jet. The filamentary flux features may represent underlying helical magnetic field lines, if we assume that the charged particles in the jet follow the wrapped magnetic field lines and radiate as they travel down the jet. This way the flux and polarization features may possibly be intertwined and de-tangling the three dimensional nature of the jet can help us understand the three dimensional magnetic field structure of the jet.

Our resulting overlay image of scatter points on the spline fit curve as well as on the polarization vector image (figures. 6 and 8), show that our model is successful in producing the three dimensional structure of the jet, based on the observed angles and distances between the any bends in the jet. We were also able to successfully reproduce the observed two dimensional structure as seen in these figures. We believe that the structure seen in our V-python images (Figure 7) is a good representation of how the actual 3 dimensional jet possibly look like, given the constraints and assumptions as explained in § 2. The angles of the bends within the jet are consistent with the possibility of filamentary nature of flux field and possibly the underlying magnetic field. From our polarimetry observations and the modeling results, it seems likely that the flux maxima in the knot D follow the magnetic field lines causing the peculiar pattern that we see. The brighter regions along the jet can be explained as the locations of higher magnetic field causing the particle acceleration and enhancing the brightness of the region as explained in Owen et al. (1989).

The apparent helical magnetic field of M87 jet has been studied extensively by various workers. Earlier in this article, we presented the optical proper motion study of M87's jet by Meyer et al. (2013), in which they present interesting results of apparent filamentary structure in different knots along the jet. Although we do not use any constraint on the proper motions in our radio data, we obtain a very similar result in terms of the filamentary structure in the flux morphology of the jet. Our radio flux and polarization images are consistent with their results obtained from the combined optical data for over 13 years. The apparent helical structure seen in knot D, A and B in their images is very similar to what we see in our polarization images of Avachat et al. (2016). On the other hand, a similar helical structure seen in our flux images also conform the possibility of presence of underlying helical magnetic field, along which the charged particles probably move producing a similar helical flux morphology, as predicted by Meyer et al. (2013) as well as some other workers as we discuss below. In the future, we plan to apply our model to the other regions of the jet especially the knots

A and B, where our polarimetry images point toward possibility of presence of an intertwined double helix. This kind of structure is also suggested by previous workers as discussed below. By adding the proper motion constraints from the results of Meyer et al. (2013) and the relativistic considerations such as angle of line of sight and observed super-luminal motions (Cheung et al. 2007), we can further restrict the ranges of unknown parameters in our model. These restrictions will also help in further understanding the differences in the morphology and hence the emission mechanisms in inner jet and outer jet of M87. We will discuss further detailed scientific interpretation of our results in paper II of this series (Avachat et al. 2017, in prep).

The JetCurry is evolving in terms of the accuracy of the results that we obtained. As discussed earlier in § 4 and shown in Figure 4, the code seems to fail on the extreme values of ϕ and ξ . The JetCurry is seem to give more accurate results in the range of larger ϕ and smaller ξ values; however, the marginal error in their values reach as high as more than 200% for $\phi > 90^\circ$ and $\xi < 20^\circ$. The reason of this possibly is a combination of the methods of non-linear solver used and the use of highly unstable trigonometric functions, such as ‘tangent’ in our model equations sets. One example of the model giving inaccurate results can be seen to be one of the sharp bends in knot D-west, shown by yellow arrow in Figure 7, bottom right panel. Upon investigation of the resultant vector for this bend, it turns out that the value of model parameter ξ is less than 20° , which clearly falls into unreliable or lower accuracy region on our code. However, given that the jets and bends within are the most unpredictable phenomena observed, by implementing a different solver and stricter boundary conditions, such as proper motion and relativistic constraints, we can optimize this code further.

For the future work, we are working on applying the relativistic constraints following the treatment of Blandford & Königl (1979). We are also working on adding the relativistic proper motion data to the non-linear equations, based on the studies of Meyer et al. (2013). The proper motion values in different regions can be used to limit the estimated parameter values in the model, whereas, the relativistic treatment will address the effects such as Doppler boosting of intensity and beaming. This will put stricter constraints on the angles and the distances between the bends. The resulting 3-D structure will thus represent a more realistic model of the jet geometry. Currently, we are using the optical flux image to solve for the geometry however, we also plan to add the radio and X-ray images and do a similar analysis. We know from our polarimetry observations that the radio, optical and X-ray electrons are possibly coming from different regions of the jet as discussed in Avachat et al. (2016). We can comment on this hypothesis by comparing the radio through X-ray 3-D images.

APPENDIX
DERIVATION OF NON-LINEAR PARAMETRIZED EQUATIONS

We consider part of a jet at a viewing angle θ , which shows an apparent bend structure as in Figure 2. A and B are neighboring knots in the jet's frame, while A' and B' are the projections of knots A and B in the sky frame with origin reference at O. The distance between A and B in the jet's frame is d , and the apparent distance between A' and B' is s . The projected bend angle relative to the x-axis in sky frame is represented as η .

Set ξ as $\angle BAC$, when $\xi < \frac{\pi}{2} - \theta$, the equation set that describes the local jet geometry is derived below: Starting with the equation of Conway & Murphy (1993) and using the geometry of Figure 2 (top), in $\triangle A'B'D'$,

$$\tan\eta = \frac{\sin\xi \sin\phi}{\cos\xi \sin\theta + \sin\xi \cos\phi \cos\theta} \quad (\text{A1})$$

where ξ , ϕ and η are the angles as shown in Figure 2 and θ is the angle of line of sight (LOS) to the observer. $\triangle AEF$ is the projection of $\triangle ABD$ onto the XY-plane (sky frame), and $\triangle ADE$ is the projection of $\triangle ABF$ onto the XZ-plane. In the right $\triangle AEF$,

$$AF = s = d \cos\beta \quad (\text{A2})$$

Because $\triangle AGH$ is the projection of $\triangle ABD$ onto the yz-plane, and $\triangle AHD$ is the projection of $\triangle ABG$ onto the XZ-plane. In the right $\triangle ABC$:

$$BG = HD = A'D' = s \cos\eta \quad (\text{A3})$$

$$s \cos\eta = d \sin\gamma \quad (\text{A4})$$

$$\gamma = \angle BAG \quad (\text{A5})$$

In the right $\triangle AGH$:

$$AG^2 = AH^2 + GH^2 \quad (\text{A6})$$

$$AH = DE = s \cos\eta \tan\alpha \quad (\text{A7})$$

$$GH = BD = B'D' = s \sin\eta \quad (\text{A8})$$

$$d^2 \cos^2\gamma = s^2 \sin^2\eta + s^2 \cos^2\eta \tan^2\alpha \quad (\text{A9})$$

Eq. A4 can be simplified by using eq. A2:

$$\cos^2\gamma = \cos^2\beta \sin^2\eta + \cos^2\beta \cos^2\eta \tan^2\alpha \quad (\text{A10})$$

Equations A3 and A5 can be combined into:

$$\left(\frac{\tan\beta}{\tan\alpha}\right)^2 = \cos^2\eta \quad (\text{A11})$$

In right triangle CID:

$$CI = DC \sin\theta = d \sin\xi \cos\phi \sin\theta \quad (\text{A12})$$

and

$$AC \cos\theta = AH + CI$$

therefore;

$$d \cos\xi \cos\theta = s \cos\eta \tan\alpha + d \sin\xi \cos\phi \sin\theta \quad (\text{A13})$$

Also, in right $\triangle ABC$,

$$AB^2 = AC^2 + BC^2$$

therefore;

$$d^2 = s^2 \left[\frac{\sin\eta}{\sin\phi}\right]^2 + s^2 \left[\frac{\cos\eta}{\cos\alpha}\right]^2 \sin^2(\theta + \alpha) \quad (\text{A14})$$

From these, we get the following set of five equations (equations A15 through A19) in five unknowns; α , β , ϕ , ξ , and d along with the measurable; η and s and assumed angle of LOS; $\theta = 15^\circ$.

$$d^2 = s^2 \left[\frac{\sin\eta}{\sin\phi}\right]^2 + s^2 \left[\frac{\cos\eta}{\cos\alpha}\right]^2 \sin^2(\theta + \alpha) \quad (\text{A15})$$

$$d \cos\xi \cos\theta = s \cos\eta \tan\alpha + d \sin\xi \cos\phi \sin\theta \quad (\text{A16})$$

$$\left(\frac{\tan\beta}{\tan\alpha}\right)^2 = \cos^2\eta \quad (\text{A17})$$

$$\tan\eta = \frac{\sin\xi \sin\phi}{\cos\xi \sin\theta + \sin\xi \cos\phi \cos\theta} \quad (\text{A18})$$

$$s = d \cos \beta \quad (\text{A19})$$

When the local jet structure has large ξ , that is when $\xi \geq \pi/2 - \theta$ (Figure 2, bottom), equations A15 and A16 above modify slightly to address the degeneracy in the geometry, as follows.

$$d^2 = s^2 \left[\frac{\sin \eta}{\sin \phi} \right]^2 + s^2 \left[\frac{\cos \eta}{\cos \alpha} \right]^2 \sin^2(\theta - \alpha) \quad (\text{A20})$$

$$d \cos \xi \cos \theta + s \cos \eta \tan \alpha = d \sin \xi \cos \phi \sin \theta \quad (\text{A21})$$

The remaining three equations, A17 through A19, stay the same for both the cases.

REFERENCES

- Astropy Collaboration, Robitaille, T. P., Tollerud, E. J., et al. 2013, *A&A*, 558, A33
- Avachat, S. S., Perlman, E. S., Adams, S. C., et al. 2016, *ApJ*, 832, 3
- Biretta, J. A., Sparks, W. B., & Macchetto, F. 1999, *ApJ*, 520, 621
- Blandford, R. D., & Königl, A. 1979, *ApJ*, 232, 34
- Broyden, C. G. 1970, *Journal of the Institute of Mathematics and Its Applications*, 6, 222
- Cheung, C. C., Harris, D. E., & Stawarz, L. 2007, *ApJL*, 663, L65
- Conway, J. E., & Murphy, D. W. 1993, *ApJ*, 411, 89
- Cormier, M. 2013, MS Thesis, U. Waterloo
- Fabian, A. C. 2012, *ARA&A*, 50, 455
- Fletcher, R. 1970, *The Computer Journal*, 13, 317
- Foreman-Mackey, D. 2016, *The Journal of Open Source Software*, 24, doi:10.21105/joss.00024
- Foreman-Mackey, D., Hogg, D. W., Lang, D., & Goodman, J. 2013, *PASP*, 125, 306
- Goldfarb, D. 1970, *Mathematics of Computation*, American Mathematical Society, 24, 23
- Hardee, P. E., & Eilek, J. A. 2011, *ApJ*, 735, 61
- Hunter, J. D. 2007, *Computing In Science & Engineering*, 9, 90
- Jones, E., Oliphant, T., Peterson, P., et al. 2001, *SciPy: Open source scientific tools for Python*
- Meier, D. L., Koide, S., & Uchida, Y. 2001, *Science*, 291, 84
- Meyer, E. T., Sparks, W. B., Biretta, J. A., et al. 2013, *ApJL*, 774, L21
- Owen, F. N., Hardee, P. E., & Cornwell, T. J. 1989, *ApJ*, 340, 698
- Pérez, F., & Granger, B. E. 2007, *Computing in Science and Engineering*, 9, 21
- Perlman, E. S., Adams, S. C., Cara, M., et al. 2011, *ApJ*, 743, 119
- Shanno, D. F. 1970, *Mathematics of Computation*, American Mathematical Society, 24, 647
- Shreher, D., Dubois, P., & Sherwood, B. 2000, *Computing in Science and Engineering*, 2, 56
- Silk, J., Antonuccio-Delogu, V., Dubois, Y., et al. 2012, *A&A*, 545, L11
- Steffen, W., Koning, N., Wenger, S., Morisset, C., & Magnor, M. 2011, *IEEE Transactions on Visualization and Computer Graphics*, Volume 17, Issue 4, p.454-465, 17, 454
- Wenger, S., Ament, M., Steffen, W., et al. 2012, *ArXiv e-prints*, arXiv:1204.6132
- Wenger, S., Lorenz, D., & Magnor, M. 2013, *Computer Graphics Forum (Proc. of Pacific Graphics PG)*, 32, 93